

MPTbreeze: A fast renormalized perturbative scheme

Martín Crocce^{1*}, Román Scoccimarro² and Francis Bernardeau³

¹*Institut de Ciències de l'Espai (IEEC-CSIC), E-08193 Bellaterra (Barcelona), Spain.*

²*Center for Cosmology and Particle Physics, Department of Physics, New York University, New York, NY 10003, USA.*

³*Institut de Physique Théorique, CEA, IPhT, F-91191 Gif-sur-Yvette, France.
CNRS, URA 2306, F-91191, Gif-sur-Yvette, France.*

2 October 2012

ABSTRACT

We put forward and test a simple description of multi-point propagators (MP), which serve as building-blocks to calculate the nonlinear matter power spectrum. On large scales these propagators reduce to the well-known kernels in standard perturbation theory, while at smaller scales they are suppressed due to nonlinear couplings. Through extensive testing with numerical simulations we find that this decay is characterized by the same damping scale for both two and three-point propagators. In turn this transition can be well modeled with resummation results that exponentiate one-loop computations. For the first time, we measure the four components of the non-linear (two-point) propagator using dedicated simulations started from two independent random Gaussian fields for positions and velocities, verifying in detail the fundamentals of propagator resummation.

We use these results to develop an implementation of the MP-expansion for the nonlinear power spectrum that only requires seconds to evaluate at BAO scales. To test it we construct six suites of large numerical simulations with different cosmologies. From these and **LasDamas** runs we show that the nonlinear power spectrum can be described at the $\lesssim 2\%$ level at BAO scales for redshifts in the range $[0 - 2.5]$. We make a public release of the **MPTbreeze** code with the hope that it can be useful to the community.

Key words: cosmological perturbation theory – cosmological parameters – baryon acoustic oscillations – large-scale structure of the universe

1 INTRODUCTION

Ongoing and future galaxy redshift surveys will render the large scale structure of the Universe with unprecedented detail thanks to a combination of redshift depth and large survey area. Among them are the Sloan Digital Sky Survey III¹, the WiggleZ survey², the Dark Energy Survey³, the Physics of the Accelerating Universe collaboration⁴ and ESA/Euclid survey⁵. The main driver underneath this effort is to seed light into the present cosmic acceleration. Various probes exist that connect different statistical aspects of galaxies properties to cosmological parameters, in particular

to those related to acceleration, such as the Baryon Acoustic Oscillations (BAO), Redshift Space Distortions (RSD) or Weak Lensing (WL). However in order to maximize the scientific outcome from this data we need to put forward precise theoretical and/or numerical predictions, for example for two-point statistics. The difficulty arise because the most rewarding range of scales lie in the nonlinear regime of structure formation.

For BAO (and RSD) these nonlinearities, due in large part to gravitational instabilities, are not strong (Eisenstein et al. 2007; Crocce & Scoccimarro 2008; Angulo et al. 2008). Hence the problem can be addressed using perturbative schemes of the equations of motion in addition to numerical N-body simulations. This is then the main goal of this paper, to propose an implementation of a (resummed) perturbative expansion for the matter power spectrum that is both accurate (percent level) and practical (few seconds of evaluation) on large BAO scales. And to have it tested as

* E-mail: martincrocce@gmail.com

¹ www.sdss3.org

² wiggles.swin.edu.au

³ www.darkenergysurvey.org

⁴ www.pausurvey.org

⁵ www.euclid-ec.org

Run	Ω_m	Ω_b	h	σ_8	n_s	$L_{box} (h^{-1} \text{ Mpc})$	N_{runs}
FID	0.27	0.04	0.7	0.9	1	1280	50
tilt					0.9	1250	4
WMAP3	0.2383	0.0418	0.73	0.74	0.95	1250	4
Low- Ω_m	0.20					1250	4
Mid- σ_8				0.8		1250	4
Low- σ_8				0.7		1250	4
LasDamas	0.25	0.04	0.7	0.8	1	2400	4

Table 1. Our suite of N-body simulations spanning different cosmological models. The top entry corresponds to our largest ensemble used as a benchmark for testing different components of the model. The last entry refers in particular to four *Oriana* runs, the largest box-size within the **LasDamas** simulations. Null entries indicate the same value as the FID run.

much as possible against numerical simulations of different cosmological models.

The process of nonlinear structure formation can be very well traced by gravitational N-body codes once certain requirements are met (e.g. Heitmann et al. (2010) and references therein). These involve, among others, good mass resolution (i.e. particle load), fine time stepping, high starting redshift, large box-size (to include long wavelength modes), etc. A percent level estimate of the power spectrum puts strong constraints in these parameters which generally slow down the numerical solver. In addition it is numerically very expensive to explore cosmological parameter space with large high resolution simulations, although efforts in this direction are currently ongoing (Heitmann et al. 2009).

In turn, cosmological perturbation theory (PT) is a well defined formalism that can be applied without extra cost to any LCDM model (and even beyond) but leads to poorly convergent results (see Bernardeau et al. (2002) for a review). One step beyond this issue was put forward by Crocce & Scoccimarro (2006a,b) through a systematic re-organization of the perturbative series so called Renormalized Perturbation Theory. This led to a better behaved expansion and more robust results (Crocce & Scoccimarro 2008). A number of similar studies with alternative methods to resum the PT expansion quickly followed, e.g. Matarrese & Pietroni (2007); Taruya & Hiramatsu (2008); Matsubara (2008); Bernardeau et al. (2008); Bernardeau & Valageas (2008); Anselmi et al. (2011) (and more recently Sato & Matsubara (2011); Elia et al. (2011); Wang & Szalay (2012) for the case of biased tracers). Overall the resulting conclusion of these works is that the matter $P(k)$ can be modeled at the percent level accuracy on weakly nonlinear scales ($k \lesssim 0.2 - 0.4 h \text{ Mpc}^{-1}$ depending on redshift), improving over standard PT. Nonetheless the structure of the solutions are complex, generally involving a set of couple integro-differential equations or multi-dimensional integrals that in any case require a time-scale of hours to evaluate.

In this paper we try to overcome this problem using an effective description of the multi-point propagators introduced in Bernardeau et al. (2008). The multi-point propagators are formally defined as the infinitesimal variation of cosmic fields with respect to the initial conditions. For Gaussian initial conditions they are equivalent to a measure of the cross correlation of final fields with initial configurations. On large scales, where PT is valid, the propagators coincide with the standard kernels in the PT expansion. To-

wards small scales nonlinear effects drive the propagators to zero (Bernardeau et al. 2008). The full dependence with time and scale is then highly non-trivial (besides the fact that formally they have a matrix structure). However the importance of the MP reside in the fact that they can be used as a well behaved expansion basis for equal time correlators such as the power spectrum, bispectrum, etc. Our effective description for the MP accounts only for most growing contributions. This, in turn, allows for a rapid evaluation of the first few terms in the MP expansion of the power spectrum. We have thoroughly tested against a large set of dedicated N-body simulations both the prescription for the different MP (and the matrix structure) as well as the resulting prediction for the nonlinear power spectrum. For all cosmologies investigated we find that our approach is able to reproduce N-body measurements at BAO scales at the $\sim 2\%$ level from low to high redshift, with evaluation times of about ten seconds.

This paper is organized as follows. In Sec. 2 we present the sets of large N-body simulations of different cosmological models used throughout the paper. In Sec. 3 we briefly recall the concept of multi-point propagators and their use as expansion basis for the nonlinear matter spectrum. Section 4 goes into more detail with the MP, comparing our effective modeling against measurements of two and three point propagators in our N-body simulations. In Sec. 5 we use these results to compute the nonlinear $P(k)$ and compare it to measurements in our fiducial ensemble, with a detailed discussion of the code performance (evaluation time, integration accuracy, etc). Sec. 6 extends this comparison to power spectrum measurements at various redshifts in our six (6) different cosmological models. Lastly, Sec. 7 contains our conclusions.

We leave for Appendix A an important discussion regarding the validity of using PT techniques derived within an Einstein - de Sitter cosmology to describe arbitrary LCDM models. We carry this out with a novel approach using numerical simulations.

2 N-BODY SIMULATIONS

We now describe the set of large N-body simulations that we developed to test our theoretical predictions. We have developed a large ensemble of high statistical significance for a fixed cosmological model and we have also carried out a set of smaller ensembles for different cosmological models.

To this later set we add measurements of $P(k)$ from some of the *LasDamas* simulations⁶.

All simulations used *Gadget2* (Springel et al. 2001) to compute the gravitational evolution, and 2nd order Lagrangian Perturbation Theory (2LPT) to set up the initial conditions at $z_i = 49$ (Scoccimarro 1998; Crocce et al. 2006).

2.1 Fiducial Cosmology

The core testing will be done against measurements in a set of 50 N-body simulations, each of comoving box-size $L_{box} = 1280 h^{-1} \text{Mpc}$ and 640^3 particles. This set then constitutes more than $100 h^{-3} \text{Gpc}^3$ of simulated volume and will be particularly important to test our model assumptions beyond two-point statistics, i.e. the three-point propagator that we discuss below.

We will refer to this set as the *fiducial cosmology* (FID). The cosmological parameters and relevant information are given in Table 1 (see Crocce & Scoccimarro (2008) for more details on the simulations). The corresponding particle mass was $m_p = 6 \times 10^{11} h^{-1} M_\odot$. We note that both the mass resolution and the settings employed to run *Gadget2* and 2LPT ensure that we achieve unbiased measurements of the power spectrum at the scales of the baryon acoustic oscillations (Heitmann et al. (2010)).

2.2 Cosmological Suite

The main goal of this paper is to provide an efficient prediction for $P(k)$ that serves across cosmological parameter space. In order to explore this we implemented numerical simulations of 5 different cosmological models in addition to the FID case, changing the parameters that are of most importance to large scale clustering such as matter density Ω_m , spectral tilt n_s , linear amplitude of fluctuations σ_8 and more. Full details are listed in Table 1.

Each cosmological model was simulated with four (4) runs of comoving box-size $L_{box} = 1250 h^{-1} \text{Mpc}$ and 640^3 particles (*Gadget2* and 2LPT settings as in the FID case above).

In addition we use some of the *LasDamas* simulations (McBride et al. 2012, in preparation). *LasDamas* is a collaborative effort that run 50 boxes of 4 different resolutions each, tailored to describing the clustering of different galaxy samples in the SDSS-II survey. Here since we are interested in large-scale clustering, we only use 4 of their largest boxes, named *Oriana*, each with 1280^3 particles within $L_{box} = 2400 h^{-1} \text{Mpc}$ (particle mass $m_p = 4.57 \times 10^{11}$). The outputs for *Oriana* sample a wide redshift range ($z = 0, 0.34, 0.52, 0.97, 1.50$ and 2.52), allowing us to test how the performance of our power spectrum prescription evolves with redshift.

2.3 Simulations with Independent Initial Positions and Velocities

Initial conditions in an N-body simulation of a given cosmological model are fully specified by initial (random) values

of particle positions and velocities, i.e. density δ and velocity \mathbf{v} perturbations⁷. Since in linear evolution the vorticity component of \mathbf{v} decays in time, the only relevant component of the velocity field is its divergence $\theta = -\nabla \cdot \mathbf{v}/\mathcal{H}f$. Moreover the linear evolution of δ and θ admits two solutions: one that grows in time (\propto to the linear growth factor) another that decays away as $H(t)$ in ΛCDM cosmology. Only the first solution survives in the long-time limit. Hence cosmological N-body simulations are always initialized already in the “growing mode”, that is, setting to zero the decaying solution by construction. This is achieved in practice by requiring that initially (minus) the divergence of the peculiar velocity field is in phase with density perturbations, i.e. $\delta_{\text{init}} = \theta_{\text{init}} = \phi$. Hence only one scalar field ϕ (randomly sampled from the linear power spectrum) determines the full realization of initial perturbations.

Here we depart from this standard practice, for the following reason. Our theoretical framework is built upon the multi-point propagators, which can be measured in simulations as the cross correlations of final and initial fields (Crocce & Scoccimarro (2006a), Bernardeau et al. (2008), Bernardeau et al. (2012))⁸. However if initial fields are in the growing mode only certain combinations in the cross correlations can be tested. For instance, the 2-point cross-correlation $r_{ab} = \langle ab \rangle$ (related to the 2-point or nonlinear propagator G_{ab}) should a priori have 4 independent combinations out of $a = (\delta_f, \theta_f)$ and $b = (\delta_i, \theta_i)$; but in practice only the projection along $\delta_i = \theta_i$ is measurable if the initial conditions are in the growing mode: $G_a = G_{ab}u_b = G_{a\delta_i} + G_{a\theta_i}$, where $u_b = (1, 1)$ indicates that the initial conditions are given by $(\delta_i, \theta_i) = (1, 1)\phi$. Thus, to date only the “density” G_δ or “velocity” G_θ two-point propagators have been tested against simulations (Crocce & Scoccimarro 2006a; Bernardeau et al. 2008, 2012).

In order to measure all the components of the propagator, and hence test our analytic predictions in much more detail, we have performed for the first time simulations with independent particle positions and velocities, leading to independent density and velocity perturbations. This was done as follows. We first generate two Gaussian random fields, $\phi_1(\mathbf{k})$ and $\phi_2(\mathbf{k})$, out of the same linear power spectrum P_0 . We then run two simulations mixing the initial conditions in densities and velocities:

$$\text{run 1} \quad \begin{cases} \delta_{\text{init}}(\mathbf{k}) = \phi_1(\mathbf{k}) \\ \theta_{\text{init}}(\mathbf{k}) = \phi_2(\mathbf{k}) \end{cases}, \quad (1)$$

and the opposite with run 2. In this way each run has initial conditions which are general in their initial values of density and velocity perturbations (hence a linear combination of growing and decaying mode solutions), such that $P_{\delta_i\delta_i}(k) = P_{\theta_i\theta_i}(k) = P_0(k)$ while $P_{\delta_i\theta_i}(k) = 0$.

At the practical level the procedure described above is equivalent to use any standard initial condition generator to produce two random sets of initial positions and velocities (out of the same linear P_0), and then combine the initial

⁶ <http://lss.phy.vanderbilt.edu/lasdamas>

⁷ By velocity perturbations we mean the velocity field after the Hubble flow at the given position has been subtracted off (the so-called peculiar velocities).

⁸ We are assuming Gaussian initial conditions in this paper, otherwise the relationship between propagators and cross-correlations is more complicated, see Bernardeau et al. (2010).

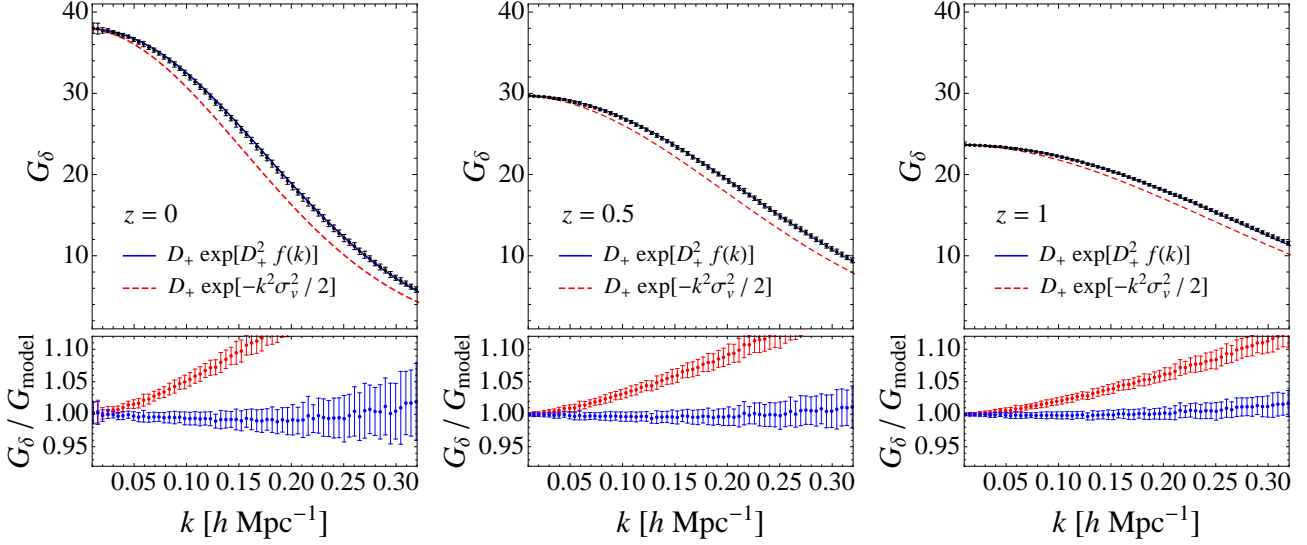


Figure 1. *Two-point (nonlinear) propagator for the density field:* model vs. measurements in N-body simulations at $z = 0, 0.5, 1$. The model in Eq. (16) performs remarkably well at all redshifts shown. The dashed line shows the corresponding high- k limit (which is only reached at very high- k , not shown here). Lower panels show the ratio of the measurements to the two different analytic descriptions and stress that the accuracy of Eq. (16) is at the percent level.

positions of the first set with the initial velocities of the second to perform the first simulation run (and viceversa for the second run). See for instance Scoccimarro (1998) for a more detailed explanation on how initial positions and velocities are set in simulations.

To some extent these two runs are not fully independent from each other, since initial positions and velocities are interchanged. We repeat the process twice so we end up with four runs of simulations with such initial conditions, our measurements below average over such four realizations.

3 MULTI-POINT PROPAGATOR EXPANSION

In this paper we will work with the so called multi-point propagator expansion of (equal-time) correlators of cosmic fields (Bernardeau et al. 2008). In particular we are interested in the nonlinear density power spectrum, which in this framework is given by

$$P_{\delta\delta}(k, z) = \sum_{r \geq 1} r! \int \delta_D(\mathbf{k} - \mathbf{q}_{1\dots r}) \left[\Gamma_{\delta}^{(r)}(\mathbf{q}_1, \dots, \mathbf{q}_r; z) \right]^2 \times P_0(q_1) \dots P_0(q_r) d^3\mathbf{q}_1 \dots d^3\mathbf{q}_r. \quad (2)$$

Here P_0 denotes the spectrum of perturbations at some initial time and $\Gamma_{\delta}^{(r)}$ are the multi-point propagators, defined as the (ensemble averaged) variation of late time cosmic fields $\Psi_a = (\delta, \theta)$ with respect to the initial conditions $\phi_a \equiv \Psi_a(z_i)$,

$$\frac{1}{r!} \left\langle \frac{\delta^r \Psi_a(\mathbf{k}, z)}{\delta\phi_{b_1}(\mathbf{k}_1) \dots \delta\phi_{b_r}(\mathbf{k}_r)} \right\rangle \equiv \delta_D(\mathbf{k} - \mathbf{k}_{1\dots r}) \Gamma_{ab_1\dots b_r}^{(r)}(\mathbf{k}_1, \dots, \mathbf{k}_r, z), \quad (3)$$

where $\mathbf{k}_{1\dots r} = \mathbf{k}_1 + \dots + \mathbf{k}_r$. In the most general scenario Eq. (2) should allow for arbitrary initial spectra of density and velocity fields P_{ab}^{init} (Bernardeau et al. 2008). But for

simplicity we have assumed that initial fields are adiabatic and in the growing mode, thus $P_{ab}^{\text{init}} = u_a u_b P_0(k)$ with $u_a = (1, 1)$. This translates into the more compact expression for the propagators

$$\Gamma_a^{(r)} \equiv \Gamma_{ab_1\dots b_r}^{(r)} u_{b_1} \dots u_{b_r}, \quad (4)$$

used in Eq. (2) evaluated for the density fluctuations ($a = 1$, or $a = \delta$). Equivalent expressions to Eq. (2) hold for $P_{\theta\theta}$ (replacing Γ_{δ} by Γ_{θ}) and $P_{\delta\theta}$ (using a cross-term $\Gamma_{\delta}\Gamma_{\theta}$).

Equation (2) results from the resummation of a whole set of (infinite) terms in the standard PT expansion of $P(k)$. Unlike the standard approach, it is a sum of positive terms each of which dominates only in a narrow range of scales. Notice that now each multi-point propagator has contributions to all orders in PT, and depend also on P_0 . At low k they can be described perturbatively while their asymptotic properties at large k can be computed beyond perturbative expansions. However, to implement in practice Eq. (2) one must have a description of multi-point propagators at all scales (and times), matching the perturbative calculations at low k to the resummed asymptotic behavior at high k . Achieving this in a way that is fast and accurate enough for the needs of cosmological surveys is the goal of our work.

The numerical evaluation of increasing orders in Eq. (2) becomes very demanding rather quickly. In order to maintain a fast evaluation time we will concentrate on quasilinear scales and implement Eq. (2) up to $r = 3$ for which we need a description of the two, three and four-point propagators. In what follows we focus in discussing the multi-point propagators in more detail, with emphasis on our particular description of $\Gamma^{(1)}$, $\Gamma^{(2)}$ and $\Gamma^{(3)}$. We then discuss in Sec. 5 the computation of the power spectrum and comparison of our predictions against measurements in simulations.

4 THE MULTI-POINT PROPAGATORS

The two-point or nonlinear propagator, first introduced by Crocce & Scoccimarro (2006b) in the context of Renormalized Perturbation Theory, is the (ensemble averaged) variation of late time cosmic fields $\Psi_a = (\delta, \theta)$ with respect to the initial conditions $\phi_a \equiv \Psi_a(z_i)$,

$$\delta_D(\mathbf{k} - \mathbf{q}) G_{ab}(k, a) = \left\langle \frac{\delta \Psi_a(\mathbf{k}, a)}{\delta \phi_b(\mathbf{q})} \right\rangle, \quad (5)$$

where we adopted the notation $G_{ab} \equiv \Gamma_{ab}^{(1)}$ and used as time variable the growth factor a^9 . This object emerged from the resummation of an infinite subset of contributions to the perturbative expansion of the power spectrum. This effectively “renormalized” the linear growth factor into a fully nonlinear and scale-dependent function: the nonlinear propagator G_{ab} . The precise way in which it is a renormalized version of the growth factor can be seen for Gaussian initial conditions, in which case G_{ab} fully describes the cross-correlation between initial and final conditions, i.e. $\langle \Psi_a \phi_b \rangle = G_{ac} \langle \phi_c \phi_b \rangle$. Also, one can easily show from Eq. (5) that an expansion of cosmic fields in terms of their initial values (as done in standard PT) leads to

$$G_{ab} = g_{ab} + \text{“nonlinear (loop) corrections”} \quad (6)$$

where g_{ab} is the standard linear propagator,

$$g_{ab}(a) = \frac{a}{5} \begin{bmatrix} 3 & 2 \\ 3 & 2 \end{bmatrix} - \frac{a^{-3/2}}{5} \begin{bmatrix} -2 & 2 \\ 3 & -3 \end{bmatrix}, \quad (7)$$

Hence, on large scales where linear PT becomes a good approximation we recover

$$G_{ab} u_b \rightarrow a \quad \text{as } k \rightarrow 0 \quad (8)$$

while on small scales nonlinear effects become dominant driving G to zero, as initial (linear) and final fields become decorrelated. In Crocce & Scoccimarro (2006a) it was shown that in this limit it is possible to resum all the dominant perturbative orders exactly, leading to

$$G_{ab}(k, a) \approx g_{ab}(a) \exp\left[-\frac{1}{2} k^2 \sigma_d^2\right] \quad \text{as } k \sigma_d \gg 1, \quad (9)$$

where the characteristic scale of decay is given by the r.m.s. one-point displacement field that to most growing order coincides with the amplitude of large-scale velocity flows,

$$\sigma_d^2 \equiv \frac{(a-1)^2}{3} \int \frac{P_0}{q^2} d^3 \mathbf{q}. \quad (10)$$

In Bernardeau et al. (2012) it has been explicitly shown that this result can be derived in a very general framework, the eikonal approximation, irrespectively of the time dependence of the large-scale flows. This partially extends the result of Anselmi et al. (2011) who were able to resum a

⁹ In what follows we will assume the structure of the theory is that of an Einstein de Sitter universe ($\Omega_m = 1$) for which the growth and scale factor coincide. The validity of the calculations is not significantly affected on large scales by this assumption if we replace a by the appropriate growth factor D_+ for the corresponding Λ CDM model. We test and discuss this in detail in Appendix A. This approach is equivalent to an approximation about the linearly decaying modes, i.e. $D_- = D_+^{-3/2}$.

sub-leading set of perturbative contributions, what led to a slight modification of the damping scale σ_d .

The importance of the high- k limit asymptotics in Eq. (9) stands from the fact that in RPT all diagrams for correlators now have the linear propagator replaced by the renormalized propagator G_{ab} inside all loops. As a result, after this resummation, large scale predictions are least sensitive to what is going on at small highly-nonlinear scales, where even the pressure-less perfect fluid approximation (used to derive these results) breaks down. This is in contrast with standard PT where, depending on the number of loops, the propagator has the wrong asymptotics, $G_{ab}(k \rightarrow \infty) \rightarrow \pm\infty$.

The two-point propagator (sometimes also called the response function) turned out important not only to RPT but also in other resummation schemes such as the Path Integral approach of Matarrese & Pietroni (2007), Closure Theory (Taruya & Hiramatsu 2008), large- N expansion (Valageas 2007a), Lagrangian schemes (Matsubara 2008) and more recently the extended TimeRG of Anselmi & Pietroni (2012). Note, however, that in some of these cases the propagator behavior at high- k can be different than in RPT and what we present here (which are in good agreement with simulations). In the Closure and Large- N cases, there are unphysical oscillations superposed with decay, whereas in the Lagrangian approach of Matsubara (2008) part of the propagator remains perturbative, and thus the same issue about violation of high- k asymptotic as in standard PT occurs.

Another key step forward was achieved in Bernardeau et al. (2008) where it was shown that the concept and results of the two-point propagator could be extended to an arbitrary number of points,

$$\frac{1}{p!} \left\langle \frac{\delta^p \Psi_a(\mathbf{k}, a)}{\delta \phi_{b_1}(\mathbf{k}_1) \dots \delta \phi_{b_p}(\mathbf{k}_p)} \right\rangle = \delta_D(\mathbf{k} - \mathbf{k}_{1\dots p}) \Gamma_{ab_1\dots b_p}^{(p)}(\mathbf{k}_1, \dots, \mathbf{k}_p, a), \quad (11)$$

where $\mathbf{k}_{1\dots p} = \mathbf{k}_1 + \dots + \mathbf{k}_p$ ¹⁰. In this case, a relation analogous to Eq. (6) is obtained

$$\Gamma_a^{(n)} = \mathcal{F}_a^{(n)} + \text{loop corrections} \quad (12)$$

where on large scales one recovers the well known $\mathcal{F}_a^{(n)} = a^n(F_n, G_n)$ kernels in PT (assuming growing mode initial conditions and keeping only the fastest growing contribution),

$$\Gamma_a^{(n)} \sim a^n \{F_n(\mathbf{k}_1, \dots, \mathbf{k}_n), G_n(\mathbf{k}_1, \dots, \mathbf{k}_n)\} \quad \text{as } k \rightarrow 0$$

for $a = 1, 2$ (density or velocity divergence fields respectively). Again, on smaller scales $\Gamma_a^{(n)}$ is expected to be driven to zero, as the p -point propagator can be shown to be proportional for Gaussian initial conditions to the cross-correlation $\langle \Psi \phi \dots \phi \rangle / P_0^p$, a generalization of the two-point result. Remarkably, the multi-point propagators also admit the resummation of the dominant behavior in the high- k limit, yielding,

$$\Gamma_a^{(n)} \rightarrow \mathcal{F}_a^{(n)} \exp\left[-\frac{1}{2} k^2 \sigma_d^2\right] \quad (13)$$

¹⁰ Note that $\Gamma^{(p)}$ denotes the $(p+1)$ -point propagator, by translation invariance it depends only on p wavenumbers in Fourier space.

in strict analogy to Eq. (9). Because of this, Eq. (2) for the power spectrum can be thought of as an expansion in terms of cross-correlations that are i) always positive and each term dominates in a narrow range of scales, ii) are well-behaved even in the nonlinear regime due to Eq. (13). The convergence of such an expansion in the nonlinear regime has been verified for the case of the Zel'dovich approximation, where the exact result is known and the expansion can be carried out to a large number of loops (Valageas 2007b).

So far we have discussed limiting expressions of the multi-point propagators in the low and high- k regimes. To continue we need prescriptions valid at all scales that can be integrated over as in Eq. (2). This will be the subject of the following sections.

4.1 Two-point (nonlinear) Propagator

We now discuss our prescription for matching the small and large k regimes of G_{ab} and thus reconstruct the full two-point propagator. The procedure is similar to that in RPT (Crocce & Scoccimarro 2006a) but is simplified because we are interested in describing the propagator at late times (unlike RPT, we will not be doing time integrations over the propagator here).

The next-to-leading order corrections to the linear propagator are given by a one-loop computation. If we neglect all sub-leading time dependencies the result reads (see Crocce & Scoccimarro (2006a) for the full expression otherwise),

$$\begin{aligned}\delta G_{11}^{\text{1loop}} &= \frac{3}{5}a^3 f(k) + \mathcal{O}(a^2) \\ \delta G_{12}^{\text{1loop}} &= \frac{2}{5}a^3 f(k) + \mathcal{O}(a^2) \\ \delta G_{21}^{\text{1loop}} &= \frac{3}{5}a^3 g(k) + \mathcal{O}(a^2) \\ \delta G_{22}^{\text{1loop}} &= \frac{2}{5}a^3 g(k) + \mathcal{O}(a^2)\end{aligned}\quad (14)$$

where

$$\begin{aligned}f(k) &= \int \frac{1}{504k^3q^5} [6k^7q - 79k^5q^3 + 50q^5k^3 - 21kq^7 \\ &+ \frac{3}{4}(k^2 - q^2)^3(2k^2 + 7q^2) \ln \frac{|k - q|^2}{|k + q|^2}] P_0(q) d^3q, \\ g(k) &= \int \frac{1}{168k^3q^5} [6k^7q - 41k^5q^3 + 2k^3q^5 - 3kq^7 \\ &+ \frac{3}{4}(k^2 - q^2)^3(2k^2 + q^2) \ln \frac{|k - q|^2}{|k + q|^2}] P_0(q) d^3q.\end{aligned}$$

Notice that both $a^2 f(k), a^2 g(k) \rightarrow -k^2 \sigma_d^2/2$ for $k \sigma_d \gg 1$. Therefore we can put together Eqs. (14) and the most-growing term in Eq. (7) and “exponentiate” the propagator as,

$$\begin{aligned}g_{11} + \delta G_{11}^{\text{1loop}} &\rightarrow G_{11} = \frac{3}{5}a \exp[a^2 f(k)] \\ g_{12} + \delta G_{12}^{\text{1loop}} &\rightarrow G_{12} = \frac{2}{5}a \exp[a^2 f(k)] \\ g_{21} + \delta G_{21}^{\text{1loop}} &\rightarrow G_{21} = \frac{3}{5}a \exp[a^2 g(k)] \\ g_{22} + \delta G_{22}^{\text{1loop}} &\rightarrow G_{22} = \frac{2}{5}a \exp[a^2 g(k)]\end{aligned}\quad (15)$$

These expressions recover the correct one-loop result at

quasi-linear scales as well as the dominant large- k asymptotic (at late times). They do not exactly match the ones given by Crocce & Scoccimarro (2006a) for RPT. Those explicitly preserved sub-leading time dependencies needed to correctly integrate the evolution from initial conditions.

For initial conditions in the growing mode, $\phi_a \propto u_a = (1, 1)$, the relevant quantity is the two-point “density” propagator $G_\delta = G_{1a}u_a = G_{11} + G_{12}$ that simply reads,

$$G_\delta(k, z) = D_+(z) \exp[f(k)D_+^2(z)] \quad (16)$$

In Fig. 1 we show how this prescription performs against measurements of the propagator in our FID ensemble of N-body simulations (top entry in Table 1)¹¹. Left, middle and right panels correspond to redshifts $z = 0, 0.5$ and 1 respectively, the model from Eq. (16) is shown in solid blue while the high- k limit expression in Eq. (9) in dashed line. Depicted error bars correspond to the variance over the ensemble. This prescription, although simple, describes the measurement at the sub-percent level at all redshifts and for all scales of interest (bottom panels in Fig. 1 show the corresponding fractional errors). In Taruya et al. (2012) a thorough analysis of the performance PT predictions at one and two-loop order is performed. It is found that for $z \gtrsim 1$ two-loop results can improve upon one-loop predictions. We stick however to one-loop prediction as given in Eq. (16) in this work as it gives predictions of ample precision in all regimes of interest. As we will see in Sec. 6 this holds true not only for our fiducial (FID) cosmology but for all the cosmological models listed in Table 1.

4.2 The Full Matrix Structure of the Propagator

As discussed in Sec. 2.3, in standard cosmological simulations initialized in the growing mode it is only possible to measure two linear combinations of the two-point propagator. In order to probe the full matrix structure (the four elements of G_{ab}) we must initialize simulations with two independent random Gaussian fields for particle positions and velocities, respectively. Let us now discuss how the resummation in the high- k limit is changed when we have independent initial density and velocity fluctuations.

A good starting point is the analysis of the structure of the one-loop contribution to G_{ab} calculated from,

$$\begin{aligned}\delta G_{ab}^{\text{1loop}} &= 4 \int_0^\eta ds_1 \int_0^{s_1} ds_2 g_{ac}(\eta - s_1) \gamma_{cde}(\mathbf{k}, \mathbf{q}, \mathbf{k} - \mathbf{q}) \\ &\times g_{df}(s_1) g_{eg}(s_1 - s_2) \times \gamma_{ghi}(\mathbf{k} + \mathbf{q}', \mathbf{q}', \mathbf{k}) \\ &\times g_{hj}(s_2) \langle \phi_f(\mathbf{q}) \phi_j(\mathbf{q}') \rangle g_{ib}(s_2)\end{aligned}\quad (17)$$

where γ_{abc} is the vertex function in standard PT (see for instance Eq. (22) in Crocce & Scoccimarro (2006a) for a general derivation of this expression), since this is what then gets exponentiated by the resummation procedure.

In the standard growing mode case the correlator of initial conditions is,

$$\langle \phi_f(\mathbf{q}) \phi_j(\mathbf{q}') \rangle = u_f u_j P_0(\mathbf{q}) \delta_D(\mathbf{q} + \mathbf{q}'), \quad (18)$$

¹¹ The measurements have been performed by cross-correlating the density field at the desired redshift with itself at the initial conditions (set in the growing mode), see Crocce & Scoccimarro (2006a) for a detailed discussion about the estimator.

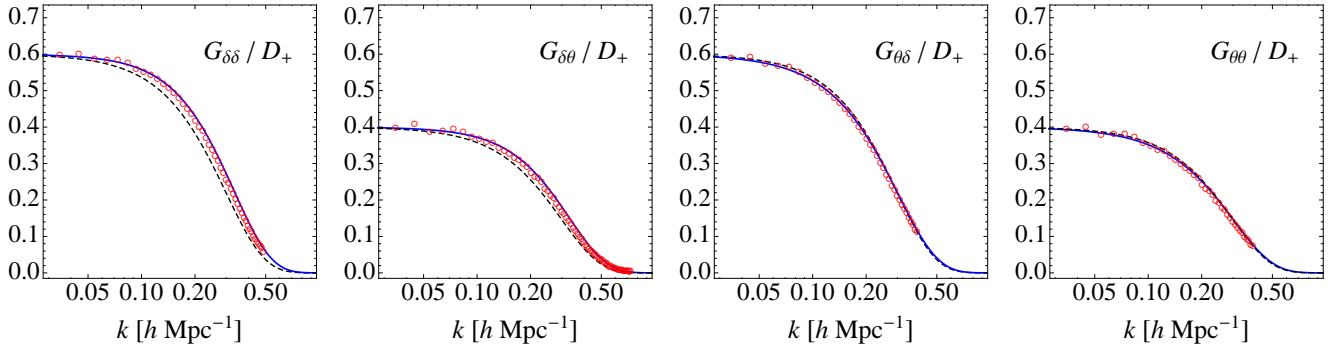


Figure 2. *Components of the Nonlinear propagator.* We show for the first time the four individual components of the nonlinear propagator (normalized to the linear growth factor) measured in dedicated simulations with independent δ and θ initial conditions. In our model the decay of the density propagators $G_{\delta\delta}$ and $G_{\delta\theta}$ is given by $\exp[(13/25)f(k)D^2(z)]$ while the velocity components $G_{\theta\delta}$ and $G_{\theta\theta}$ are given by $\exp[(13/25)g(k)D^2(z)]$, see Eqs. (15,22). Dashed lines show for reference the decay obtained in the high- k limit $\exp(-k^2(13/25)\sigma_d^2/2)$ (same for all).

with $u = (1, 1)$. For our mixed mode initial conditions we have instead (see Sec. 2.3),

$$\langle \phi_f(\mathbf{q})\phi_j(\mathbf{q}') \rangle = \delta_{fj}^K P_0(\mathbf{q})\delta_D(\mathbf{q} + \mathbf{q}'), \quad (19)$$

where the Kronecker symbol $\delta_{fj}^K = 1$ if $f = j$ and 0 otherwise. This means that instead of evaluating

$$g_{df}(s_1)g_{hj}(s_2)u_f u_j = e^{s_1+s_2}u_d u_h \quad (20)$$

in the standard case (with $s = \ln a$), we have to compute

$$g_{df}(s_1)g_{hj}(s_2)\delta_{fj}^K = \frac{13}{25}e^{s_1+s_2}u_d u_h + \text{decaying mode}, \quad (21)$$

where the decaying mode piece evolves as $e^{-3(s_1+s_2)/2}$. Therefore, neglecting the decaying mode contribution we see that the overall effect of using independent random field initial conditions is to renormalize

$$\{f(k), g(k)\} \rightarrow \frac{13}{25} \{f(k), g(k)\} \quad (22)$$

in Eqs. (14). This can be carried out to all orders leading to the same high- k limit resummation as Eq. (16) except that

$$\sigma_d^2 \rightarrow \frac{13}{25}\sigma_d^2. \quad (23)$$

Thus our model for the full propagator for independent δ and θ initial conditions is simply the one in Eqs. (15) with the replacement given in Eq. (22).

In Fig. 2 we show the four different components of the propagator measured in the simulations with independent δ and θ initial conditions against predictions by the above model (in solid blue) and the high- k asymptotic (in dashed black). The propagator was measured following,

$$G_{ab}(k) = \frac{\langle \Psi_a(\mathbf{k})\phi_b(-\mathbf{k}) \rangle}{P_0(k)} \quad (24)$$

where now the initial conditions ϕ_b are different for density ($b = 1$) or velocities ($b = 2$) according to Eq. (1). The velocity divergence fields in Eq. (24) were estimated following the procedure describe in Scoccimarro (2004). Reassuringly all the four components follow the expected theoretical decay towards small scales. This is an interesting and important cross-check, in particular for resummation schemes such as RPT or Closure Theory, that integrate the individual components separately rather than the “density” and “velocity”

propagators that until this paper were the only combinations tested against simulations.

4.3 Three and Four-Point Propagators

The three-point propagator was introduced by Bernardeau et al. (2008) and recently studied in detail in Bernardeau et al. (2012). In the later work a general scheme (called **RegPT**) to interpolate between small and large scale information for any propagator was proposed. In particular, the **RegPT** prescription for the three-point propagator is given by,

$$\Gamma_a^{(2)\text{RegPT}}(\mathbf{k}_1, \mathbf{k}_2) = \left[\Gamma^{(2)\text{Tree}}(\mathbf{k}_1, \mathbf{k}_2) + \delta\Gamma^{(2)\text{one-loop}}(\mathbf{k}_1, \mathbf{k}_2) + \frac{1}{2}k^2\sigma_d^2\Gamma^{(2)\text{Tree}}(\mathbf{k}_1, \mathbf{k}_2) \right] \exp(-k^2\sigma_d^2/2) \quad (25)$$

where $\mathbf{k} = \mathbf{k}_1 + \mathbf{k}_2$. Here $\Gamma^{(2)\text{Tree}}$, $\delta\Gamma^{(2)\text{one-loop}}$ and σ_d depend on time. The one-loop term in this expression is described in detail in Bernardeau et al. (2012) and involves one integral over $P_0(q)$ for each triangle configuration $(\mathbf{k}_1, \mathbf{k}_2)$. Although Eq. (25) gives a very good agreement with measurements in simulations we have found that its usefulness to compute the one-loop $P(k)$ is limited because it takes a long time to evaluate. We hence seek an alternative prescription.

We have found that, in analogy to Eq. (16), the following expression ($\mathbf{k} = \mathbf{k}_1 + \mathbf{k}_2$)

$$\Gamma_\delta^{(2)}(\mathbf{k}_1, \mathbf{k}_2; z) = D_+^2(z) F_2(\mathbf{k}_1, \mathbf{k}_2) \exp[f(k)D_+^2(z)] \quad (26)$$

yields very similar results to that in Eq. (25) and virtually the same one-loop power spectrum after the corresponding momentum integration. Figure 3 shows measurements of $\Gamma^{(2)}$ for different triangle configurations together with the prediction by the model in Eq.(26) in solid black (used throughout this paper) and **RegPT** from Eq. (25) in dashed black. Left and Middle panels correspond to *equilateral* with $k_1 = k_2 = k_3 = k$ (top left); *colinear* with $k_1 = k_2 = k/2$ and $k_3 = k$ (top center); *elongated* (bottom left) with $k_1 = k/2$

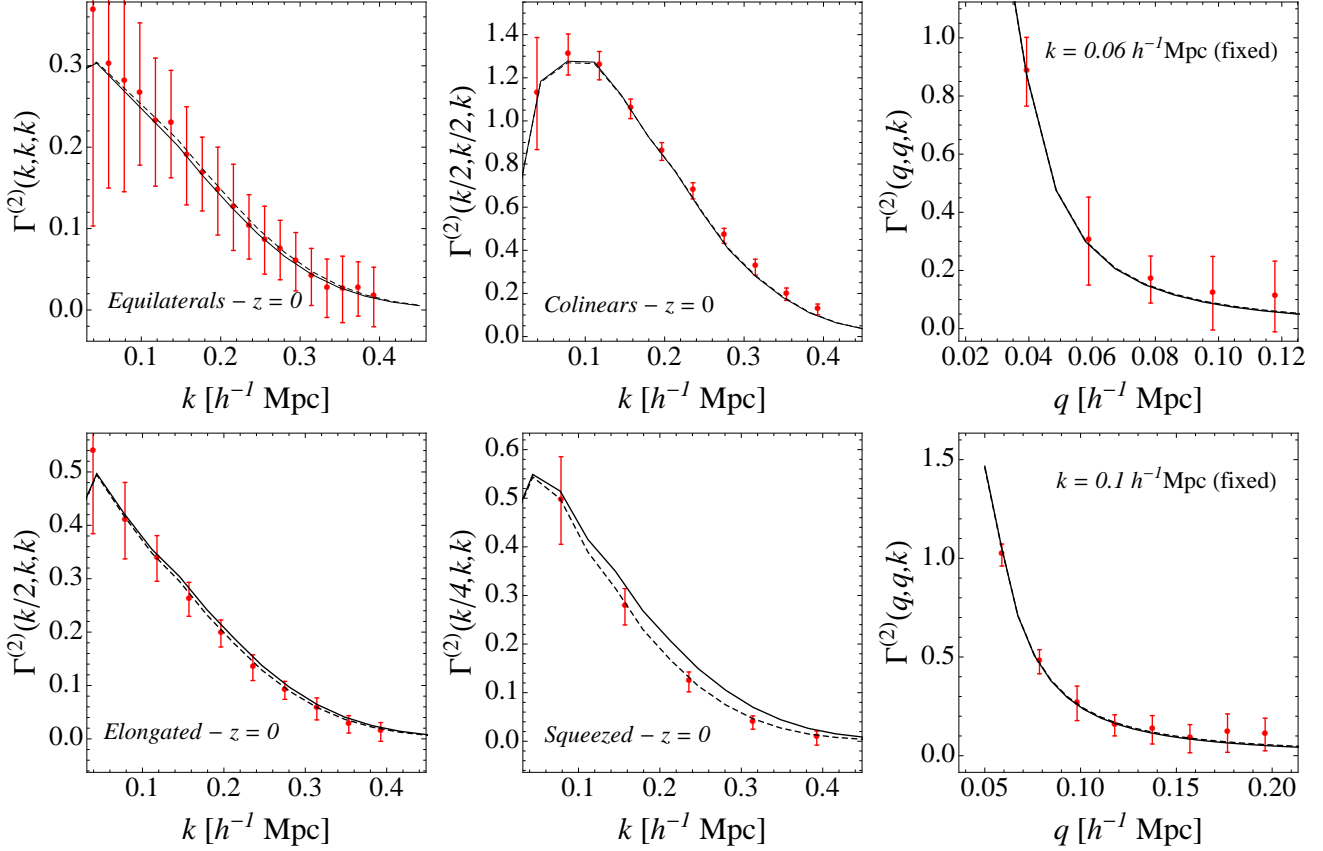


Figure 3. *Nonlinear three-point propagator: analytic predictions vs. measurements.* Different panels show measurements of $\Gamma^{(2)}(q_1, q_2, q_3)$ in our fiducial ensemble of simulations for different triangular configurations, as indicated in the y-axis label (see text for details). Solid line corresponds to the interpolation scheme proposed in this paper, see Eq. (26). Dashed line to the one introduced in Bernardeau et al. (2011) (**RegPT**), see Eq. (25). They are mostly indistinguishable for almost all configurations and agree with the measurements remarkably well. In particular for right panels where we show the configuration that contribute the most to the one-loop power spectrum at (fixed) wavenumber $k = 0.06 h^{-1} \text{ Mpc}$ ($0.1 h^{-1} \text{ Mpc}$). Error bars correspond to the variance over the ensemble and results (in left and middle panels) are plotted against $k_3 = k$.

and $k_2 = k_3 = k$; and *squeezed* (bottom center) $k_1 = k/4$ $k_2 = k_3 = k$ configurations¹².

Notice that the theory is binned in the same way as the data, this is essential to recover the correct asymptotic behavior at low- k (see Bernardeau et al. (2012) for details on the $\Gamma^{(2)}$ estimator and the binning correction).

From these panels it is clear that both models perform very well for all these configurations with a slight over-prediction by Eq. (26) for squeezed configurations.

In addition the right panels of Fig. (3) show the same comparison for the configuration that would yield the dominant contribution to the one-loop computation of $P(k)$. From Eq. (2) we see that the one-loop power spectrum is

of the form

$$P^{\text{1loop}}(k) \sim \frac{4\pi}{k} \int P_0(q_1) q_1 dq_1 \int P_0(q_2) q_2 dq_2 \times \left[\Gamma_{\delta}^{(2)}(q_1, q_2, k) \right]^2 \quad (27)$$

Hence by symmetry reasons the most relevant configuration for a given k is roughly $\Gamma^{(2)}(q, q, k)$. Figure (3) shows this configuration for $k = 0.06 h \text{ Mpc}^{-1}$ (top right panel) and $k = 0.1 h \text{ Mpc}^{-1}$ (bottom right panel). Here again the model in Eq.(26) describes the N-body results remarkably well yielding the same answer as **RegPT** (notice the dashed and solid line are on top of each other).

The four-point propagator is basically a measure of the trispectrum between final and initial density fields. Thus it is difficult to measure from the N-body simulations. Nonetheless from theoretical grounds we do know the behavior at low and high- k , and have no reason to expect a different behavior at intermediate scales from the one already probed for the two and three-point propagators. Hence we will adopt

¹² We assume the final (nonlinear) density field has wave-vector k_3 (last argument). Hence the three-point propagator is only symmetric with respect to the 1st and 2nd indices that corresponds to the initial (linear) fields.

the following prescription ($\mathbf{k} = \mathbf{k}_{123}$),

$$\Gamma_\delta^{(3)}(\mathbf{k}_1, \mathbf{k}_2, \mathbf{k}_3; z) = D_+^3(z) F_3(\mathbf{k}_1, \mathbf{k}_2, \mathbf{k}_3) \exp[f(k) D_+^2(z)], \quad (28)$$

for the four-point propagator, in full analogy to Eqs. (16) and (26). This prescription will then satisfy the low- k and high- k asymptotics.

Provided with prescriptions for the propagators up to four points, we are now ready to discuss the multi-point expansion for the power spectrum.

5 POWER SPECTRUM

In this section we present the prescriptions we adopt to do the actual computations of the power spectra. We call **MPTbreeze** this implementation and comment at the end of the section on possible alternative approaches.

To describe the power spectrum at mildly nonlinear scales we implemented the first three terms in the expansion in Eq. (2). In diagrammatic language they correspond to renormalized versions of tree level, one and two loops respectively (by renormalized we mean that the renormalized propagators include themselves loops to all orders). The tree-level term is simply given by

$$P_{\text{tree}} = [\Gamma^{(1)}(k, z)]^2 P_0 \quad (29)$$

and coincides with the propagator renormalization term of RPT (Crocce & Scoccimarro 2006b). Here $\Gamma_\delta^{(1)}$ is given by Eq. (16) and P_0 is the linear, post-recombination, spectrum of fluctuations. This term is the one that contain most information on narrow band features of the primordial perturbations such as the Baryon Acoustic Oscillations. The “mode-coupling” contributions start with the next term in Eq. (2) that reads,

$$P_{1\text{-loop}}(k, z) = 2 \int d^3 \mathbf{q} [\Gamma_\delta^{(2)}(\mathbf{k} - \mathbf{q}, \mathbf{q}; z)]^2 P_0(|\mathbf{k} - \mathbf{q}|) P_0(q) \quad (30)$$

Assuming \mathbf{k} along the z -axis it can be easily turn into

$$P_{1\text{-loop}}(k, z) = 4\pi \int_{-1}^1 dx \int dq [\Gamma_\delta^{(2)}(p, q, y; z)]^2 P_0(p) P_0(q)$$

where $x = \mathbf{k} \cdot \mathbf{q} / (k q)$ and we have introduced $\mathbf{p} = \mathbf{k} - \mathbf{q}$ and $y = \mathbf{p} \cdot \mathbf{q} / (p q)$ for clearness. Here $\Gamma_\delta^{(2)}$ is given by Eq. (26) with $F_2(p, q, y) = \frac{5}{7} + \frac{y}{2} \left(\frac{q}{p} + \frac{p}{q} \right) + \frac{2y^2}{7}$ the standard 2nd-order PT kernel (e.g. Bernardeau et al. (2002)). We are then left with an integration in 2-dimensions which can be rapidly evaluated with a standard Gaussian quadratures routine.

The third term in Eq. (2) is slightly more involved but can be treated similarly, we now have

$$P_{2\text{-loop}}(k, z) = 6 \int d^3 \mathbf{q}_1 \int d^3 \mathbf{q}_2 [\Gamma_\delta^{(3)}(\mathbf{k} - \mathbf{q}_{12}, \mathbf{q}_1, \mathbf{q}_2; z)]^2 P_0(|\mathbf{k} - \mathbf{q}_{12}|) P_0(q_1) P_0(q_2). \quad (31)$$

Here we can take k along the z -axis and \mathbf{q}_1 in the $x - z$,

$$\begin{aligned} \mathbf{k} &= k (0, 0, 1) \\ \mathbf{q}_1 &= q_1 (\sin \theta, 0, \cos \theta) \\ \mathbf{q}_2 &= q_2 (\sin \phi \sin \alpha, \cos \phi \sin \alpha, \cos \alpha), \end{aligned}$$

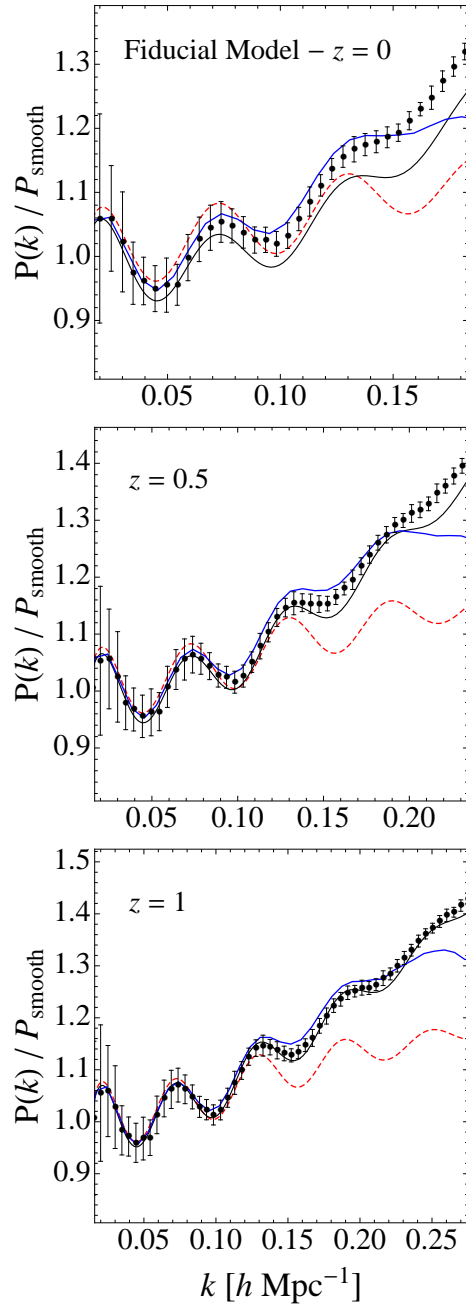


Figure 4. The multi-point propagator expansion presented in this paper (solid blue line) against measurements of $P(k)$ in our FID ensemble of N-body simulations (top entry in Table 1) at $z = 0, 0.5$ and 1 . The dotted red line is linear theory and solid black is **halofit**. The evaluation time of the multi-point expansion shown in each panel is at most five seconds.

so we are then left with the following 5-dimensional integral

$$P_{2\text{-loop}}(k, z) = 12\pi \int dq_1 \int dq_2 \int dx \int dy \int d\phi [\Gamma_\delta^{(3)}(\mathbf{q}_3, \mathbf{q}_1, \mathbf{q}_2; z)]^2 P_0(q_3) P_0(q_1) P_0(q_2) \quad (32)$$

where we introduced $\mathbf{q}_3 = \mathbf{k} - \mathbf{q}_{12}$; $x = \cos \theta = \mathbf{k} \cdot \mathbf{q}_1 / (k q_1)$ and $y = \cos \alpha = \mathbf{k} \cdot \mathbf{q}_2 / (k q_2)$ are integrated in $[-1, 1]$ and ϕ , the azimuthal orientation of \mathbf{q}_2 , in $[0, 2\pi]$. The propagator

$\Gamma_\delta^{(3)}$ is given by Eq. (28) in terms of $f(k)$, Eq. (15), and F_3 , which in turn is solved iteratively in terms of (F_2, G_2) (see e.g. Bernardeau et al. (2002)).

It should be noted that all the required integrals safely converge for any realistic shape of the matter power spectrum. The regularization scale σ_d is finite as soon as the power spectrum is steeper than k^{-1} in the low wave-mode limit ($n > -1$). All terms involved in the computation of the power spectrum actually require the same conditions in the IR domain. The convergence in the UV domain is more diagram dependent. The condition for the existence of σ_d demands that $n < -1$ if n is the power spectrum index at large wave-modes. The convergence properties of $P_{1\text{-loop}}(k, z)$ and $P_{2\text{-loop}}(k, z)$ are all determined by the behavior of the $\gamma_{abc}(\mathbf{k}, \mathbf{q}, \mathbf{k} - \mathbf{q})$ (symmetrized) vertex functions, introduced in Eq. (17). They obey the scaling relation,

$$\gamma_{abc}(\mathbf{k}, \mathbf{q}, \mathbf{k} - \mathbf{q}) \sim \frac{k^2}{q^2}, \quad (33)$$

when $q \gg k$. As in the expressions of $P_{1\text{-loop}}(k, z)$ and $P_{2\text{-loop}}(k, z)$, two such factors are introduced in the high q limit, the convergence of the former is secured as soon as $n < 1/2$ and that of the latter when $n < -2/3$. It therefore does not lead to new constraints besides the existence of σ_d . This is at variance with the convergence properties of the multi-loop corrections to the two-point propagators. They indeed lead to much stringent constraints in the UV domain as discussed in Taruya et al. (2012). We will comment further on the consequences of those properties in Sec. 5.2.

To perform the integration of Eq. (32) we employ a MonteCarlo algorithm routine called *Vegas* (Lepage 1978, 1980), included within the v1.4 CUBA library of multidimensional numerical integration routines described in Hahn (2005)¹³. This is discussed in more detail in Sec. 5.1.

We are now ready to compute the model prediction and compare it with measurements in N-body simulations. Figure 4 shows the two-loops multipoint expansion in solid blue line, linear theory in dotted red and *halofit* (Smith et al. 2003) in solid black, at $z = 0, 0.5$ and 1 (top to bottom panels). Symbols with error bars are the corresponding measurements of $P(k)$ in our fiducial cosmological model (error-bars correspond to the variance over the ensemble of 50 simulations, see Table 1). All lines are divided by a smooth broad-band linear spectrum to reduce the y -axis dynamic range. Overall, the multi-point expansion match the measurements at the 2% – 3% level up to scales $k \sim 0.16 h \text{ Mpc}^{-1}, 0.19 h \text{ Mpc}^{-1}, 0.23 h \text{ Mpc}^{-1}$ at $z = 0, 0.5$ and 1 respectively. These values coincide roughly with σ_d^{-1} at the given redshift, with σ_d given by Eq. (10). Notice also that these scales are slightly beyond the Baryon Acoustic Oscillations region. Improving upon this $\sim 2\%$ accuracy requires a more precise ansatz for the multi-point propagators, in particular for $\Gamma^{(3)}$ because it dominates within this region ($k \gtrsim 0.1 h \text{ Mpc}^{-1}$).

We have also investigated whether the addition of the next term in the expansion of Eq. (2), that corresponds to a 3-loop computation, extends the agreement to higher wave-modes. The result is that it does but only slightly because

of the already strong exponential suppression of the corresponding five-point propagator. In turn, the numerical evaluation of the 3-loop integral becomes very lengthy. An alternative path is to combine our PT approach with halo model prescriptions, in the spirit of Valageas & Nishimichi (2011). This will be the subject of future work.

For our FID cosmology we have checked that the recent ansatz by Tassev & Zaldarriaga (2012) under-estimates the N-body measurements by 4% at $z = 0$, gives a $\sim 1\%$ match at $z = 0.5$ and over-estimates $P(k)$ by $\sim 2\%$ at $z = 1$ (at BAO scales). This ansatz is based upon a split between long and short wave-modes, which was somewhat arbitrarily chosen to be a sharp k -cutoff at $\Lambda = k/2$. The strength of nonlinear corrections in the model, hence also the above residuals, depends (systematically with redshift) on Λ .

5.1 MPTbreeze: Code performance and convergence

The major advantage of the method presented in the previous section is that the evaluation time is of the order of a few seconds, comparable to that of linear Boltzman codes used to compute the transfer function of different species. This is opposed to resummation techniques such as RPT and Closure Theory that take significantly longer times to compute. Hence our approach it is very well suited for sampling the large-scale structure likelihood of present and future datasets at BAO scales.

In addition note that due to the structure of the expansion the same evaluation done for a given redshift can be properly re-scaled to another one at almost no extra cost, just recomputing G and the corresponding growth factor.

It seems then appropriate to discuss the performance of the code in more detail and the numerical convergence. Clearly, the component that is numerically intensive to evaluate is the 5 dimensional “2-loop” integration given in Eq. (32). As mentioned before we have performed it with the Monte Carlo algorithm *Vegas* that uses importance sampling as a variance-reduction technique.

The accuracy of the integration, and hence the evaluation time, is controlled by setting the required absolute ε_{abs} and relative ε_{rel} errors¹⁴ (Hahn 2005).

For $\varepsilon_{\text{rel}} = 1\%$ (with $\varepsilon_{\text{abs}} = 0$) the full computation of the $z = 1$ power spectrum including tree, one and two loops in steps of $\delta k = 0.005 h \text{ Mpc}^{-1}$ (roughly the fundamental mode in our simulations) up to $k_{\text{max}} = \sigma_d^{-1} = 0.244 h \text{ Mpc}^{-1}$ (49 bins) *evaluates in only 5 secs*. The same integration with $\varepsilon_{\text{rel}} = 0.5\%$ requires 10 secs and roughly 3 minutes for $\varepsilon_{\text{rel}} = 0.1\%$. Moreover, we find that generally the three accuracies yield the same power spectrum to a sub-percent level thus $\varepsilon_{\text{rel}} = 1\%$ (the fastest) seems a reasonable choice.

A similar test at $z = 0.5$ is even quicker because the validity of the expansion is more limited. Now $k_{\text{max}} = \sigma_d^{-1} = 0.195 h \text{ Mpc}^{-1}$ (39 bins) *evaluates in just ~ 3 secs*. setting $\varepsilon_{\text{rel}} = 1\%$ (7 secs. with $\varepsilon_{\text{rel}} = 0.5\%$). Notice that all the timings reported are for single CPU (and the code compiled with the Intel compiler *ifort*).

In all cases the numerical integration in momentum

¹³ Publicly available at <http://www.feynarts.de/cuba/>

¹⁴ Convergence is achieved once the estimation \hat{I} of the integral I satisfies $|\hat{I} - I| \leq \max(\varepsilon_{\text{abs}}, \varepsilon_{\text{rel}} I)$

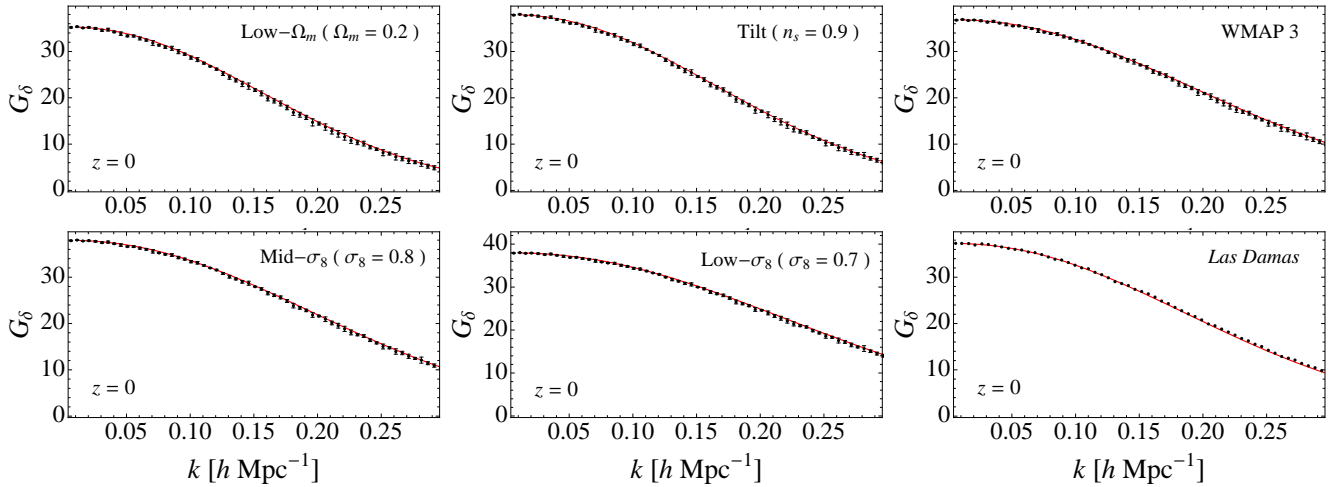


Figure 5. Nonlinear two-point propagator at $z = 0$ for different cosmological models. In each panel symbols with error bars correspond to the measurements of the propagator over four simulations of the given cosmology. In solid red lines we show the prescription used throughout this paper corresponding to the exponentiation of the most-growing one-loop contribution: $D_+ \exp [D_+(z)^2 f(k)]$. It agrees with the measurements at the sub-percent level for all the scales of interest in all cases studied.

space is done from a fixed $q_{min} \sim 10^{-4}$ up to some cut-off scale q_c . A priori the box-sizes of our simulations are large enough that wave-modes longer than L_{box} have negligible amplitude to alter the measured power spectrum in the simulations. Hence we assume no finite box-size effect and take q_{min} arbitrarily small. On the other hand we find that we need $q_c \sim 1 h \text{ Mpc}^{-1}$ in order for the integrals to converge within 0.5%. This mild sensitivity to the ultraviolet (UV) cut-off is due to the particular prescription for MP adopted here, with the decay standing as an overall multiplicative function ($\Gamma^{(n)} = G(k) \times F_n$) that factors out of loop integrals such as Eqs. (30,31). This is unlike approaches such as RPT where the full nonlinear propagator is integrated inside all loops, what screens much strongly the UV regime where e.g. shell-crossing enters (and convergence is achieved already for $q_c \sim 0.5 h \text{ Mpc}^{-1}$).

Lastly we have also performed our integrals with other Monte Carlo algorithms implemented within the CUBA library, reaching always the same answer obtained with Vegas but employing more time to converge. For example *Suave* (importance sampling with globally adaptive subdivisions) employs 1 minute 25 seconds to evaluate the $z = 1$ spectrum for $\varepsilon_{rel} = 0.005$. *Divonne* (Friedman & Wright 1981a,b), which uses stratified sampling, requires 61 seconds for the same task. As described above, *Vegas* is substantially faster requiring only 10 seconds (or less for higher ε_{rel}).

5.2 MPTbreeze compared to RegPT

It is possible to construct alternative implementations of MP resummations. **RegPT** is an alternative proposition that relies on slightly different choices for the computation of the multi-point functions and on numerical implementations (Taruya et al. 2012). Let us first stress that to a large extent both approaches share the same advantages and disadvantages: the power spectrum is constructed out of a sum of positive terms and each of these terms could be computed on its own; the resulting power spectrum exhibits a large- k cutoff which

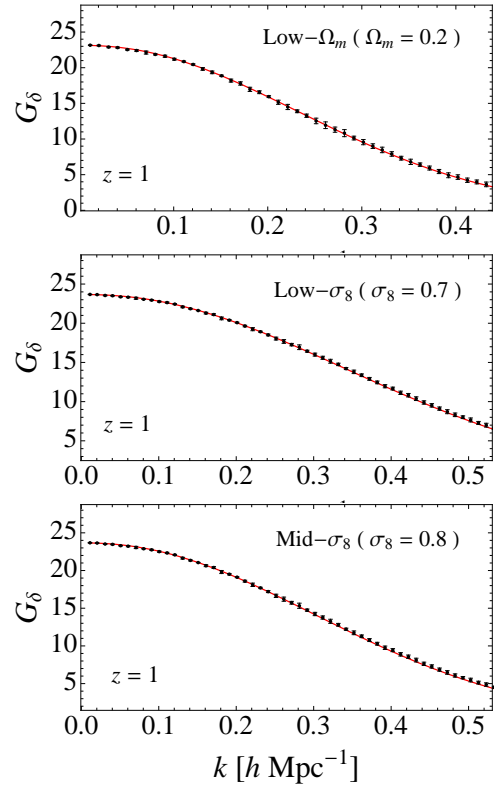


Figure 6. Same as Fig. 5 but at $z = 1$ (and for three cosmological models). The simple model for G_δ (solid red line) still performs at the sub-percent level in all scales and models.

signals the limit of the validity range of the computation. The main difference in the implementations comes from the fact that, in the **RegPT** case, all two loop order terms are taken into account following the prescription proposed in Bernardeau et al. (2012) in the computation of the propagators. This is not the case in this work where the loop

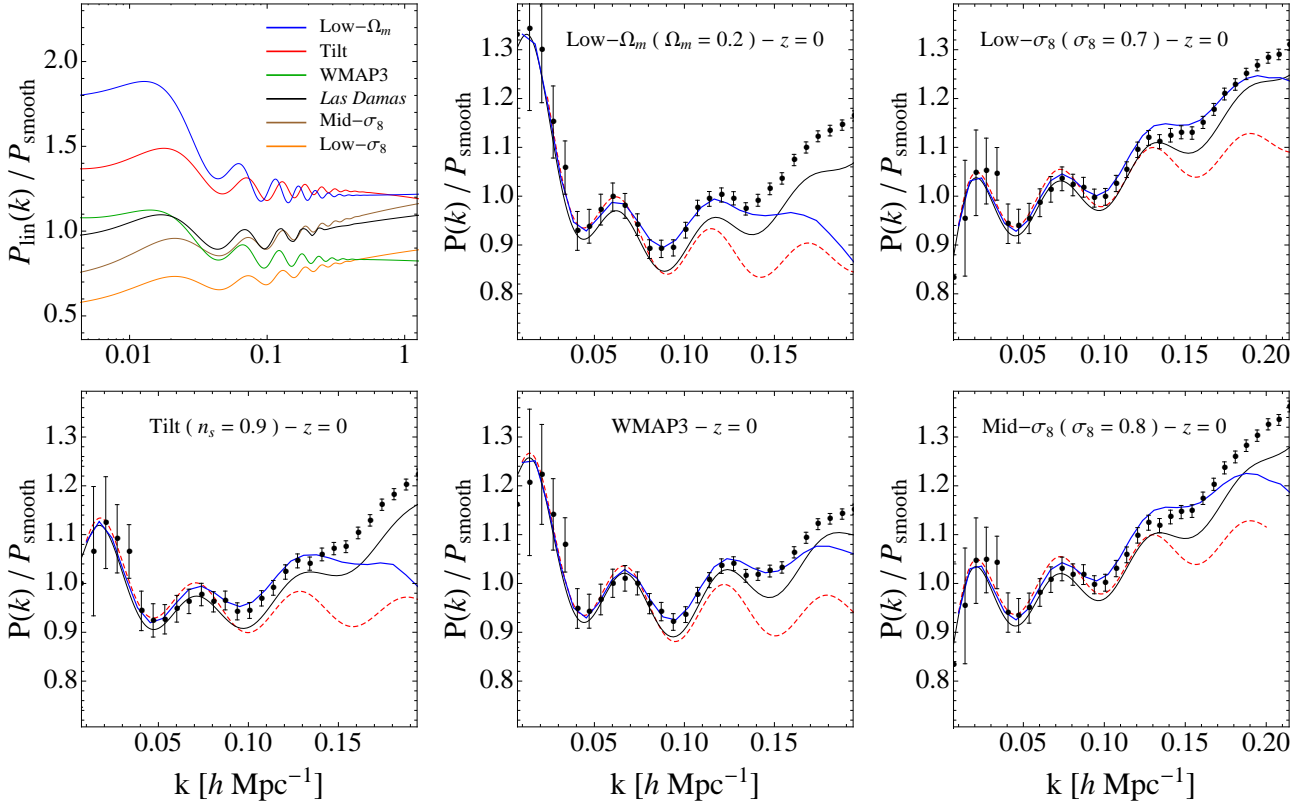


Figure 7. Power spectrum performance for different cosmological models at $z=0$. Top left panel shows the linear power spectra in each of the simulated cosmologies divided by a smooth broad-band power. Remaining panels show measurement of $P(k)$ over four independent simulations for each model. We used the same P_{smooth} (except for its normalization) for all panels. In these panels dashed red lines correspond to linear theory, black solid lines to **halofit** and solid blue lines to the multi-point expansion presented in this work (see text for more details). The latter is found accurate at the $\sim 2\%$ level on BAO scales throughout all cosmologies investigated.

corrections to the propagators are computed with a more phenomenological approach.

Because of these differences, the computational difficulties of the two approaches vary. The computation of the expression (30) when the one-loop correction to $\Gamma^{(2)}$ is taken into account reveals quite costly for a direct computation. The **MPTbreeze** implementation avoids this difficulty. Even with direct Monte-Carlo integrations it is then possible to obtain the results within a very short time¹⁵.

The other main difference concerns the converging properties of the involved diagrams. As shown in Sect. 5, diagrams involved in the **MPTbreeze** computations have good converging properties. In practice, for wave modes of the order of $0.1\text{--}0.5\ h/\text{Mpc}$ the results depend on wave modes that are of comparable scales. This is not necessarily the case for the **RegPT** implementation. As it will be stressed in a forthcoming paper, the two-loop corrections to the two-point propagator are sensitive in particular to wave-modes well

above a few $h\ \text{Mpc}^{-1}$. The use of these two-loop corrections improves upon the two-point propagator predicted value at least for $z \gtrsim 1$ so that **RegPT** predictions can be potentially more precise. But it also makes the predictions less robust with regards to the overall spectrum as it makes the results more sensitive to nonlinear scales where baryon physics and shell crossings are likely to significantly affect the growth of structure.

6 MULTI-POINT EXPANSION VS. N-BODY FOR VARYING COSMOLOGICAL MODELS

In this section we extend the testing of the multi-point expansion beyond the fiducial cosmological model used so far to measurements in our dedicated set of N-body simulations of various cosmologies described in Table 1. This kind of study is important given the number of assumptions leading to, say, Eqs. (29,30,31). It also helps setting in robust terms the validity and usefulness of our approach. Our results are summarized in Figs. 5, 6, 7 and 8.

A clear picture of the different scenarios investigated is given in the top-left panel of Fig. 7 where we show the ratio of linear spectra of the simulated cosmologies to a reference

¹⁵ In Taruya et al. (2012), it will be shown that it is possible to considerably shorten the CPU time required to compute the diagram involved in the **RegPT** prescription with the use of a “fast” algorithm. The latter is based on the use of precomputed kernel functions making possible the computation of diagrams in ~ 0.01 secs. per mode. We note that such a procedure can also be applied in the context of **MPTbreeze**.

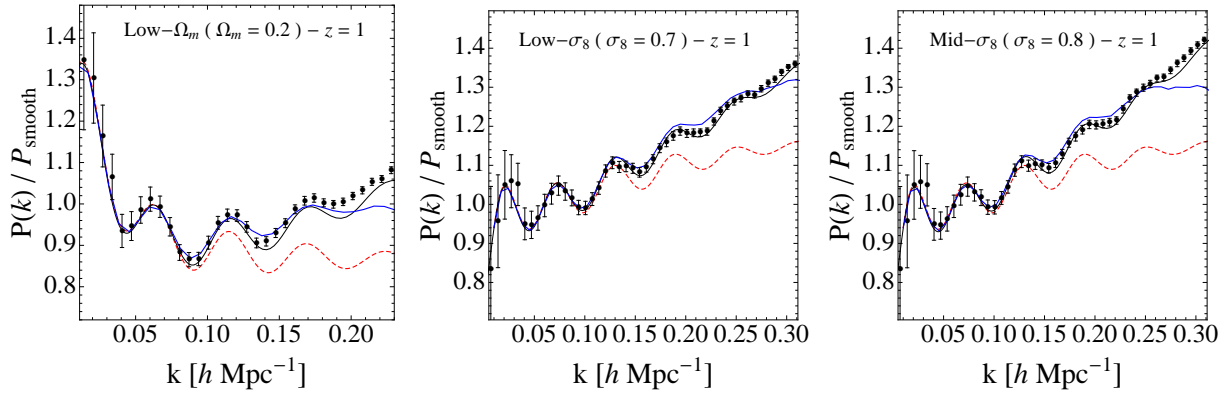


Figure 8. Power spectrum performance for different cosmologies at $z = 1$. Symbols correspond to simulation measurements, dashed red lines to linear theory, black solid to **halofit** and blue solid to the multi-point expansion, which remains accurate at $\lesssim 2\%$ on at least all scales showing Baryon Acoustic Oscillations.

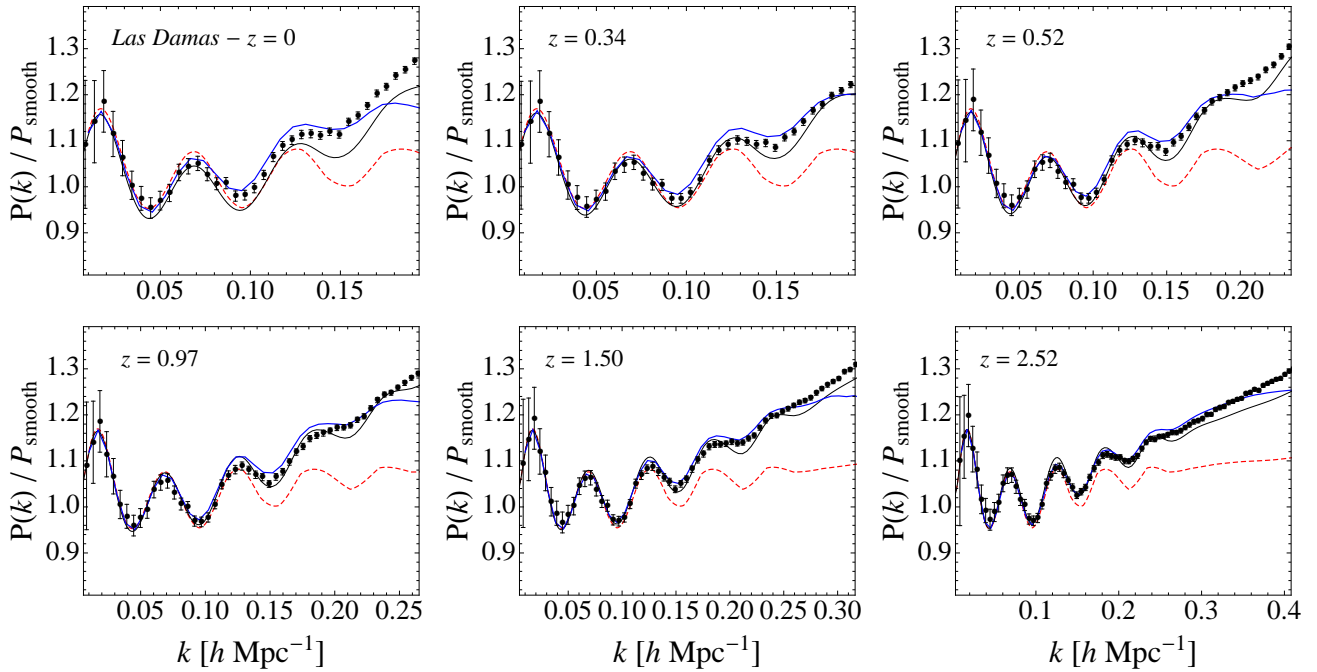


Figure 9. Performance of the model presented in this paper for **Las Damas** cosmology (detailed in Table 1) as a function of redshift. Data points with error bars are the measurements in three runs of Oriana. Solid blue are the predictions by the multi-point expansion (this work), while red dashed and solid black corresponds to linear theory and **halofit** respectively.

smooth power¹⁶. The amplitude of the longest wavelength modes (i.e. $P^{1/2}$) varies by up to 70%, and a similar spread is found for the effective tilt at $k \sim 0.01 h \text{ Mpc}^{-1}$.

Let us first concentrate in the prediction for the two-point propagator given in Eq. (16) for the different cosmological models and its comparison to simulation measurements. This is depicted in Fig. 5 for propagators measured at $z = 0$ and Fig. 6 for those at $z = 1$. Remarkably in all cases the

simple model given in Eq. (16) performs at the sub-percent level for all the scales of interest, at least up to $z = 1$.

We now turn to the analysis of power spectrum prediction using multi-point expansion for all the cosmological models detailed in Table 1. Figures 7 and 8 show the measured power spectrum at $z = 0$ and $z = 1$ respectively. Solid blue line is the two-loop model from Eqs. (29-31), solid black corresponds to **halofit** and dashed red to linear theory.

At both $z = 0$ and $z = 1$ the multi-point expansion perform as for the FID case, that is, it matches the measurements up to $k \sim \sigma_d^{-1}(z)$ (for the given cosmology) at the $\lesssim 2\%$ level. This means, broadly speaking, up to $k = 0.15 h \text{ Mpc}^{-1}$ at $z = 0$ and $k = 0.25 h \text{ Mpc}^{-1}$ at $z = 1$.

¹⁶ The smooth baseline used throughout the paper is a BBKS transfer function (Bardeen et al. 1986) of shape $\Gamma = 0.135$ with tilt $n_s = 0.99$ and arbitrary normalization.

In turn **halofit** works at the $\lesssim 6\%$ level. In some cases, however, this departure appears at rather low k (e.g. for low- Ω_m).

In Fig. 9 we concentrate in the performance of our implementation of the multi-point expansion as a function of redshift, from low z to high z using **LasDamas** measurements as a benchmark. **Halofit** seems to perform best around $z \sim 1$ but for smaller and higher redshifts departs more substantially from the measurements. For example, at $z = 0$ **Halofit** is suppressed compared to simulations by 5% at $k = 0.15 h \text{ Mpc}^{-1}$ and 8% at $k = 0.3 h \text{ Mpc}^{-1}$. Using **Halofit** as a benchmark for PT calculations is therefore not accurate enough for present-day work (Crocce & Scoccimarro 2008). It may be for this reason that Carrasco et al. (2012) find a strong effect due to shell crossing at weakly nonlinear scales, after checking their effective stress tensor reproduces **Halofit** for the **LasDamas** cosmology. In fact, in earlier work Pueblas & Scoccimarro (2009) characterized the impact of a non-zero stress tensor and concluded that (extrapolating to the **LasDamas** cosmology at $z = 0$), shell crossing effects are about 1% (2%) at $k = 0.2$ (0.3) $h \text{ Mpc}^{-1}$ (see also Pietroni et al. (2012)). This justifies ignoring these effects in the calculations we present here at the scales of validity of **MPTbreeze** (note that as shown in Pueblas & Scoccimarro (2009) the effects of shell-crossing are strongly redshift-dependent, thus at $z > 0$ they are less of a concern).

It is worth stressing here that in all cases the performance of our code is maintained at a few seconds, as in the FID case described in Sec. 5.1.

Error bars shown in all power spectrum figures correspond to the expected statistical error (variance of the band power spectra) for the given simulation box-size. We have found that using only four realizations to estimate this error can be very unreliable. One needs at least ten or more runs to estimate this robustly (we have performed this testing using our 50 FID runs). Instead we found that the FKP expression (Feldman et al. 1994) below matches the resulting ensemble error in our large FID ensemble very well on the scales we are interested ($k \lesssim 0.4 h \text{ Mpc}^{-1}$)

$$\frac{\sigma_P}{P} = \sqrt{\frac{2}{(4\pi k^2 \delta k)/k_f^3}}, \quad (34)$$

where δk is the particular binning used in the P estimation and $k_f = 2\pi/L_{\text{box}}$. Hence we use Eq. (34) to depict error estimates in Figs. 7, 8 and 9.

In Figs. (4,7,8 9) we have decided to show, besides **MPTbreeze** results, those from tools with comparable functionality such as **halofit**. We have nonetheless tested that RPT, as detailed in Crocce & Scoccimarro (2008), is also accurate at the percent level but in a broader range of scales. However this is at the expense of longer evaluation times (hours as opposed to seconds).

In addition we note that a fitting formulae for the nonlinear power spectrum that updates **halofit** is available, the Coyote Universe emulator (Lawrence et al. 2010). However, this emulator can only be used within a specific region of parameter space which unfortunately exclude all the cosmologies investigated in our paper, even the one of **LasDamas**. This is mostly because the Coyote emulator does not treat h as an independent variable, but rather as one fixed by the distance to the large scattering surface as measured by

CMB. Hence in Figs. 7, 8 and 9 we can only show the estimates from **halofit**.

7 CONCLUSIONS

With **MPTbreeze** we have implemented a renormalized perturbative approach for the nonlinear power spectrum, the so called multi-point propagators expansion. We put particular emphasis on the description of the BAO range of scales from low to high redshift. The main advantage over other techniques already present in the literature is that the evaluation time is of the order of 5-10 seconds (in a single CPU), as discussed in Sec. 5.1.

Our implementation is based on a phenomenological description of the multi-point propagators themselves. In particular how their scale-dependence interpolates between their perturbation theory forms at low- k and their large- k behavior obtained from non-perturbative re-summations. For the two-point (nonlinear) propagator at late times there is an unambiguous way to do this interpolation through well-known one-loop results, this is discussed in Sec. 4.1.

We compared the adopted prescription with propagator measurements in N-body simulations for seven different cosmological models (listed in Table 1 and discussed in more detail below). Remarkably we find it always gives a sub-percent agreement for all scales of interest, as shown in Figs. 1, 5 and 6. In addition, we developed simulations with independent initial positions and velocities. This allowed us to test for the first time the full matrix structure of the two-point propagator. We found that all individual components show an exponential suppression towards small scales, in turn very well reproduced by our simple prescription (see Fig. 2).

We then moved to the three-point propagator $\Gamma^{(2)}$ that is a function of triangle configurations. Hence its description is a priori much more complex. Recently Bernardeau et al. (2012) put forward an interpolation scheme that respects the low- k at arbitrary loop order and the high- k limit. Evaluating this would require one-loop calculations of $\Gamma^{(3)}$, which we find slow to integrate numerically. Instead, we found that the decay of the three-point propagator when compared to measurements in N-body simulations is to a large extent the same as for the two-point case described above (in turn much faster to evaluate). In particular for configurations relevant for $P(k)$ calculations, see Fig. 3.

Provided with these results for the multi-point propagators we implemented the MP expansion in Eq. (2) for the nonlinear power spectrum. In parallel we developed a set of large N-body simulations of different cosmological models. Given the number of approximations in implementing a practical approach, testing against different cosmological models seems the only route to establish robust conclusions. The top-left panel of Fig. 7 gives an idea of the different slopes and amplitudes of the linear spectrum simulated in this paper.

Comparison of $P(k)$ measurements at various redshifts and cosmological models and our theory modeling is presented in Figs. 7, 8, 9. Overall we can establish the accuracy of our approach at the 2% level on weakly nonlinear scales (roughly up to σ_d^{-1} , given in Eq. 10). It always improves over standard PT and **halofit**. As mentioned above the evalu-

ation time scale remains around 5 to 10 secs. depending on redshift, integration accuracy, etc.

Probably the main disadvantage of our implementation is that the range of validity does not extend much beyond BAO scales, particularly a low- z . This can be overcome by interpolating weakly nonlinear scales, as described by our approach, with high- k asymptotic given by halo models (Valageas & Nishimichi 2011) or $P(k)$ resummation techniques (Anselmi & Pietroni 2012). We leave this extra construction for future work.

The code used to compute the multipoint expansion presented in this work is publicly available at <http://maia.ice.cat/crocce/mptbreeze/>.

8 ACKNOWLEDGEMENTS

Some of the simulations presented here are part of the **LasDamas** collaboration suite and were run thanks to a Teragrid allocation and the use of RPI and NYU computing resources. Funding for this project was partially provided by the Spanish Ministerio de Ciencia e Innovación (MICINN), project AYA2009-13936, Consolidar-Ingenio CSD2007-00060, European Com-missions Marie Curie Initial Training Network CosmoComp (PITN-GA-2009-238356), research project 2009-SGR-1398 from Generalitat de Catalunya and the Juan de la Cierva MEC program. RS acknowledges support by grants NSF AST-1109432 and NASA NNA10A171G and FB acknowledges support by the French *Programme National de Cosmologie et Galaxies*. We thank Pablo Fosalba for comments on the draft.

REFERENCES

- Angulo R. E., Baugh C. M., Frenk C. S., Lacey C. G., 2008, *Mon. Not. R. Astr. Soc.* , 383, 755
- Anselmi S., Matarrese S., Pietroni M., 2011, *Journal of Cosmology and Astroparticle Physics*, 6, 15
- Anselmi S., Pietroni M., 2012, ArXiv e-prints 1205.2235
- Bardeen J. M., Bond J. R., Kaiser N., Szalay A. S., 1986, *Astrophys. J.* , 304, 15
- Bernardeau F., Colombi S., Gaztanaga E., Scoccimarro R., 2002, *Phys. Rep.* , 367, 1
- Bernardeau F., Crocce M., Scoccimarro R., 2008, *Phys. Rev. D* , 78, 103521
- Bernardeau F., Crocce M., Scoccimarro R., 2012, *Phys. Rev. D* , 85, 123519
- Bernardeau F., Crocce M., Sefusatti E., 2010, *Phys. Rev. D* , 82, 083507
- Bernardeau F., Valageas P., 2008, *Phys. Rev. D* , 78, 083503
- Bernardeau F., van de Rijdt N., Vernizzi F., 2012, *Phys. Rev. D* , 85, 063509
- Carrasco J. J. M., Hertzberg M. P., Senatore L., 2012, ArXiv e-prints 1206.2926
- Crocce M., Pueblas S., Scoccimarro R., 2006, *Mon. Not. R. Astr. Soc.* , 373, 369
- Crocce M., Scoccimarro R., 2006a, *Phys. Rev. D* , 73, 063520
- Crocce M., Scoccimarro R., 2006b, *Phys. Rev. D* , 73, 063519

- Crocce M., Scoccimarro R., 2008, *Phys. Rev. D* , 77, 023533
- Eisenstein D. J., Seo H.-J., White M., 2007, *Astrophys. J.* , 664, 660
- Elia A., Kulkarni S., Porciani C., Pietroni M., Matarrese S., 2011, *Mon. Not. R. Astr. Soc.* , 416, 1703
- Feldman H. A., Kaiser N., Peacock J. A., 1994, *Astrophys. J.* , 426, 23
- Friedman J. H., Wright M. H., 1981a, SLAC Report CGTM-193-REV, CGTM-193
- Friedman J. H., Wright M. H., 1981b, ACM Trans. Math. Software, 7, 76
- Hahn T., 2005, Computer Physics Communications, 168, 78
- Heitmann K., Higdon D., White M., Habib S., Williams B. J., Lawrence E., Wagner C., 2009, *Astrophys. J.* , 705, 156
- Heitmann K., White M., Wagner C., Habib S., Higdon D., 2010, *Astrophys. J.* , 715, 104
- Hiramatsu T., Taruya A., 2009, *Phys. Rev. D* , 79, 103526
- Lawrence E., Heitmann K., White M., Higdon D., Wagner C., Habib S., Williams B., 2010, *Astrophys. J.* , 713, 1322
- Lepage G. P., 1978, J. Comp. Phys., 27, 192
- Lepage G. P., 1980, Report CLNS-80/447, Cornell Univ., Ithaca, N.Y.
- Matarrese S., Pietroni M., 2007, Journal of Cosmology and Astro-Particle Physics, 6, 26
- Matsubara T., 2008, *Phys. Rev. D* , 77, 063530
- McDonald P., Trac H., Contaldi C., 2006, *Mon. Not. R. Astr. Soc.* , 366, 547
- Pietroni M., 2008, Journal of Cosmology and Astro-Particle Physics, 10, 36
- Pietroni M., Mangano G., Saviano N., Viel M., 2012, *Journal of Cosmology and Astroparticle Physics*, 1, 19
- Pueblas S., Scoccimarro R., 2009, *Phys. Rev. D* , 80, 043504
- Sato M., Matsubara T., 2011, *Phys. Rev. D* , 84, 043501
- Scoccimarro R., 1998, *Mon. Not. R. Astr. Soc.* , 299, 1097
- Scoccimarro R., 2004, *Phys. Rev. D* , 70, 083007
- Scoccimarro R., Colombi S., Fry J., Frieman J., Hivon E., Melott A., 1998, *Astrophys. J.* , 496, 586
- Smith R., Peacock J., Jenkins A., White S., Frenk C., Pearce F., Thomas P., Efstathiou G., Couchman H., 2003, *Mon. Not. R. Astr. Soc.* , 341, 1311
- Springel V., Yoshida N., White S. D. M., 2001, New Astronomy, 6, 79
- Taruya A., Bernardeau F., Nishimichi T., Codis S., 2012, ArXiv e-prints 1208.1191
- Taruya A., Hiramatsu T., 2008, *Astrophys. J.* , 674, 617
- Tassev S., Zaldarriaga M., 2012, *Journal of Cosmology and Astroparticle Physics*, 4, 13
- Valageas P., 2007a, *Astr. & Astrophys.* , 465, 725
- Valageas P., 2007b, *Astr. & Astrophys.* , 476, 31
- Valageas P., Nishimichi T., 2011, *Astr. & Astrophys.* , 527, A87
- Wang X., Szalay A., 2012, *Phys. Rev. D* , 86, 043508

APPENDIX A: THE EDS APPROXIMATION

The derivation of the multi-point expansion as presented in Bernardeau et al. (2008) assumes that the cosmological model is such that $\Omega_m(\tau)/f_+(\tau)^2 = 1$, where $f_+(\tau) = d \ln D_+(\tau) / d \ln a$ and $D_+(\tau)$ is the growing mode solution

for the density contrast of the *linearized* equations of motion: $\delta(\mathbf{k}, \tau) = D_+(\tau)\delta_0(\mathbf{k})$.

In this approximation the equations of motion simplify considerably reducing basically to the ones in an Einstein de Sitter background ($\Omega_m = 1$) with a factorized linear growth factor, i.e. replacing the one in EdS, $a(\tau)$, for the corresponding $D_+(\tau)$ (see Scoccimarro et al. (1998)). Then at each perturbative order the solution becomes separable in τ and \mathbf{k} with the corresponding most growing term satisfying $D_n = (D_+)^n$ and the PT kernels reducing to the ones in an EdS Universe.

This approximation is known to be very accurate because for most of the cosmic evolution $\Omega_m \sim 1$. It is usually followed in standard perturbation theory as well in resummed approaches such as those in Crocce & Scoccimarro (2006b), Valageas (2007a), Matarrese & Pietroni (2007), Taruya & Hiramatsu (2008) and Matsubara (2008).

Pietroni (2008) investigated its limitations by numerically integrating a system of coupled differential equations involving the power spectrum and bispectrum (see also Hiramatsu & Taruya (2009)). Here we follow an alternative approach implementing numerical simulations to directly address the validity of this approximation, in particular at BAO scales where we expect our analytical model to yield percent-level predictions. A different testing using numerical simulations is presented in McDonald et al. (2006).

From the theoretical point of view the approach described above amounts to say that all the (nonlinear) cosmological evolution is set by the linear growth factor D_+ . Hence two cosmological models with the same linear spectrum (normalized at say $z = 0$) will show the same nonlinear $P(k)$ at times τ_1 and τ_2 such that $D_{+, \text{model 1}}(\tau_1) = D_{+, \text{model 2}}(\tau_2)$.

Hence we did the following numerical experiment: provided with our fiducial Λ CDM run for $\Omega_m = 0.27$ started at $z_i^{\Lambda\text{CDM}} = 49$. We implemented a complementary CDM simulation ($\Omega_m = 1$) started at a time that matched the growth from the initial conditions in the Λ CDM case. This yielded $z_i^{\text{CDM}} = 37$. We chose outputs for the Λ CDM at $z = 0, 0.3$ and 1 with corresponding growth from the initial redshift $D_+ = 38, 32.78$ and 23.66 . Thus we output the $\Omega_m = 1$ CDM run at times that matched these growth factors, $z = 0, 0.159$ and 0.605 . We then compared the measured power spectrum and two-point propagator in the Λ CDM run with the corresponding “matched growth” one in the CDM case. If the approximation were perfect these ratios would be 1.

Results are shown in Fig. A1 for the redshifts mentioned above. Top panel corresponds to the power spectrum comparisons and bottom to the nonlinear two-point propagator.

As expected on the largest scales (where linear theory applies) the ratio is indeed unity. At high z (where Ω_m is closer to 1) the ratio is still unity within 0.2% for $k \lesssim 0.4 h \text{ Mpc}^{-1}$. In turn, at low z the approximation does break down towards small scales. Nonetheless BAO scales are mostly unaffected. For instance, at $k \lesssim 0.2 h^{-1} \text{ Mpc}$ and $z = 0.3$ ($z = 0$) the CDM power is $\lesssim 0.5\%$ ($\lesssim 1\%$) smaller than the Λ CDM one. Pietroni (2008) finds similar deviations but a factor of two smaller (0.5% error at $z = 0$ and $k \sim 0.2 h \text{ Mpc}^{-1}$).

In any case the approximation is found accurate at the sub-percent level on large BAO scales at low- z with extended validity at higher z and smaller scales.

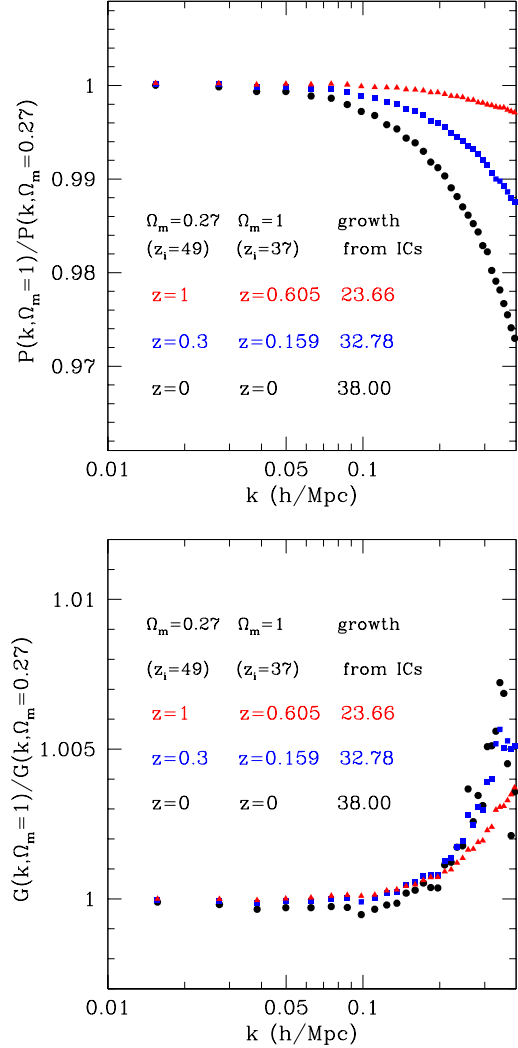


Figure A1. An approximate solution of the PT equations of motion (at each order) for an arbitrary Λ CDM background is obtained by solving the CDM case with a time dependence given by the linear growth of the Λ CDM model, i.e. changing $a(\tau) \rightarrow D_+(\tau)$. We test this approximation here by running “growth matched” simulations of similar Λ CDM and $\Omega_m = 1$ CDM models (except by their value of Ω_m). The top panel shows the relative difference in the measured power spectra and the bottom panel the ratio of nonlinear two-point propagators. The approximation is weakest at low- z but it is always never worse than 1% at BAO scales.